Hindawi
Shock and Vibration
Volume 2024, Article ID 9854631, 1 page
https://doi.org/10.1155/2024/9854631

Retraction

Retracted: Study on the Failure Mechanism of Strain Rockburst

Shock and Vibration

Received 23 January 2024; Accepted 23 January 2024; Published 24 January 2024

This article has been retracted by Hindawi following an investigation undertaken by the publisher [1]. This investigation has uncovered evidence of one or more of the following indicators of systematic manipulation of the publication process:

(1) Discrepancies in scope

(2) Discrepancies in the description of the research reported

(3) Discrepancies between the availability of data and the research described

(4) Inappropriate citations

(5) Incoherent, meaningless and/or irrelevant content included in the article

(6) Manipulated or compromised peer review

The presence of these indicators undermines our confidence in the integrity of the article's content and we cannot, therefore, vouch for its reliability. Please note that this notice is intended solely to alert readers that the content of this article is unreliable. We have not investigated whether authors were aware of or involved in the systematic manipulation of the publication process.

Wiley and Hindawi regrets that the usual quality checks did not identify these issues before publication and have since put additional measures in place to safeguard research integrity.

We wish to credit our own Research Integrity and Research Publishing teams and anonymous and named external researchers and research integrity experts for contributing to this investigation.

The corresponding author, as the representative of all authors, has been given the opportunity to register their agreement or disagreement to this retraction. We have kept a record of any response received.

References

[1] L. Zhou, G. Wang, R. Hu et al., "Study on the Failure Mechanism of Strain Rockburst," *Shock and Vibration*, vol. 2022, Article ID 1663350, 12 pages, 2022.

Hindawi
Shock and Vibration
Volume 2022, Article ID 1663350, 12 pages
https://doi.org/10.1155/2022/1663350

Research Article

Study on the Failure Mechanism of Strain Rockburst

Lichao Zhou,[1] **Gang Wang**,[2,3] **Rong Hu**,[4] **Xiqi Liu**,[3] **Dongxing Wang**,[3] **Leibo Song**,[2] **and Yong Niu**[2]

[1]*Zhengzhou Shengda University, Zhengzhou 451191, China*
[2]*School of Civil Engineering, Shaoxing University, Shaoxing 312000, China*
[3]*Key Laboratory of Geotechnical and Structural Engineering Safety of Hubei Province, School of Civil Engineering, Wuhan University, Wuhan 430070, China*
[4]*School of Civil Engineering, University of South China, Hengyang 421001, China*

Correspondence should be addressed to Gang Wang; gangw277842@whut.edu.cn

Received 26 May 2022; Accepted 20 June 2022; Published 11 July 2022

Academic Editor: Pengfei Wang

Among the factors affecting rock mass failure, the stress state has the greatest influence on the mechanical behavior of rock. The mechanical behavior of rock depends on the change of stress path, and the stress of rock mass is closely related to deformation and failure. In order to study the influence of surrounding rock stress state on the failure mode of surrounding rock, based on the theory of elastic mechanics and fracture mechanics, this paper analyzed the stress state of surrounding rock element and crack propagation of surrounding rock, and estimated the potential failure mode of surrounding rock in different areas of a phosphate mine in Yichang. The results showed that: the surrounding rock element is affected by the gradient stress, and a larger stress gradient corresponds to a larger principal stress ratio and variation direction of the surrounding rock. The failure mode of surrounding rock is affected by the coupling effect of principal stress ratio and principal stress direction. Under the action of certain crack angle and appropriate confining pressure, different fracture mechanisms may occur in the surrounding rock compression. But the partition of surrounding rock failure mode region can predict the surrounding rock failure mode to a certain extent.

1. Introduction

Strain rock burst is caused by tangential stress concentration of surrounding rock after excavation of high in-situ stress rock mass. In the process of underground tunnel construction and excavation [1, 2], different types of rock bursts often occur, and the corresponding failure phenomenon and failure form of different types of rock bursts are different [3, 4].

Huang [5] summarized the basic rules of rock burst occurrence in tunnels according to rock burst data of Erlang Mountain Road tunnel. When the sound of cracking and tearing is emitted inside the tunnel surrounding rock, the cracks occur in parallel walls and only involve the surface surrounding rock of the tunnel, accompanied by the crack and stripping of thin flake, lenticular and plate debris, and no ejection phenomenon occurs. When there is a dull burst sound inside the surrounding rock, the sound is feeble, the burst surrounding rock is mostly lenticular, ribbed plate, block, etc., with ejecting phenomenon, and the fracture is mostly wedge or arc concave cavity.

Lipeng Liu et al. [6] summarized more than 110 rock burst data of Jinping II hydropower station, and summarized its laws from the characteristics of rock burst development process and rock burst damage phenomenon. When the rock burst debris is flake- or plate-like, the intensity of rock burst is relatively small, and the surrounding rock debris is mainly distributed near the wall of the adit, the throwing phenomenon is not obvious, and the fracture surface is relatively straight, showing tensile failure. However, the burst ejection rock burst has a higher intensity and is characterized by sudden and violent throwing of debris, accompanied by air waves and sound characteristics. The corresponding rock burst pit surface is dome-shaped and

wedge-shaped, generally coarse and with fine rock powder, and in the surrounding rock generally occurs a shear failure.

Wang et al. [7], according to the Jinping hydropower station tunnel engineering field rock burst phenomenon investigation, summarized the shear failure occurs rock burst mechanism of surrounding rock, shear failure occurs, the adit wall first wedge-shaped forms a potential failure structure, surrounding rock concentrates stress, shear wedge accumulates elastic strain energy, when the shear stress on the potential failure surface exceeds the shear strength of the rock mass, the wedge is thrown out and rock burst is formed. The fragments of this kind of rock burst are thrown over a long distance.

Zhao et al. [8] pointed out that the failure mode and fracture mechanism of rock fracture correspond to the macroscopic fracture characteristics and intensity level of rock burst site to a certain extent, that is, the tensile failure caused by intergranular fracture or cleavage fracture of rock mass is mainly slight rock burst, mostly manifested as lamellar and lamellar spalling. However, the shear failure caused by rock fragmentation or transgranular fracture is violent and the rock burst intensity is high. According to the deformation rock burst failure phenomenon above, it can be seen that the strain rock burst intensity is related to the failure type of surrounding rock, and different proportions of brittle fracture modes will lead to the difference of rock burst failure evolution forms. In order to explore the formation mechanism of rock burst surrounding rock with different failure modes, based on the theory of elastic mechanics and fracture mechanics, this paper analyzes the stress state and crack propagation of the surrounding rock. The results have important theoretical and engineering guiding significance in rock burst mechanism, rock burst tendency prediction, and risk assessment of jointed surrounding rock.

2. Analysis of the Factors Affecting the Failure of Surrounding Rock of Strain Rock burst

Among the factors affecting rock mass failure, the stress state has the greatest influence on the mechanical behavior of rock, which depends on the change of stress path, and the stress of rock mass is closely related to deformation and failure [8]. After rock mass excavation, the tangential stress of surrounding rock is larger in the tunnel wall and decreases in a certain gradient to the inside of surrounding rock until it tends to the original rock stress. The gradient distribution of tangential stress in surrounding rock not only affects the principal stress ratio of rock elements, but also produces shear stress between elements and leads to the deflection of stress principal axis. Stress ratio and principal stress direction are the controlling factors of fracture propagation direction and crack properties. Based on the analysis and summary of in-situ deformation rock burst phenomenon, this chapter classifies the corresponding types of deformation rock burst from the perspective of surrounding rock failure mode. Based on the analysis of the influencing factors of the corresponding variant rock burst, the stress state and the variation of the failure mode of surrounding rock are described by elastic mechanics and fracture mechanics.

2.1. Influencing Factors of Tunnel Surrounding Rock Failure Mode. There are many factors leading to the formation of different types of strain rock burst. However, no matter how complex its internal mechanism is, rock burst is mainly controlled by two factors, namely lithological conditions and stress field conditions [9–13]. It is found that the deep rock mass is mostly hard brittle rock mass, which generally meets the requirements of lithological conditions when rock burst occurs. Therefore, in order to essentially understand the generation process of different types of rock burst, the brittle fracture characteristics of surrounding rock should be further analyzed from the perspective of the stress characteristics of rock mass before and after excavation. As shown in Figure 1, from the perspective of stress state, the main factors affecting fracture generation, propagation and fusion are as follows: (1) principal stress ratio (σ_3/σ_1); (2) direction of principal stress action.

After excavation of deep rock mass, according to the stress law of surrounding rock mass, the radial stress of surrounding rock mass is zero at the wall of the adit, and tends to the original rock stress in the interior of surrounding rock. The tangential stress of surrounding rock mass is larger in the wall and decreases to the interior of surrounding rock with a certain gradient. Therefore, the failure mode of rock burst surrounding rock mass under this stress state is affected by the principal stress ratio and principal stress direction. As the tangential and radial stresses of surrounding rock change together, the principal stress ratio of surrounding rock increases gradually from the wall to the interior of surrounding rock. The gradient distribution of radial and tangential stress of surrounding rock will lead to the shear stress of adjacent rock elements, and then, the principal stress direction will be deflected to different degrees, resulting in different crack evolution laws in the failure process of surrounding rock.

Figure 2 reflects the influence of principal stress ratio on failure mode of surrounding rock. As shown in Figure 2, the principal stress ratio (σ_3/σ_1) leads to changes in the rock fracture pattern and between brittleness and ductility. When the principal stress ratio of surrounding rock is small, the brittle failure of surrounding rock element mainly occurs. With the increase of the principal stress ratio of the confining rock mass, the failure mode gradually changes from tensile failure to shear failure. As shown in Figure 3 , when the principal stress ratio exceeds a certain value, the rock failure mode of the surrounding rock gradually changes from brittle failure to ductile failure. After the excavation, the principal stress ratio increases gradually from the wall to the interior of the surrounding rock, and the failure modes of rock mass in different areas of the corresponding surrounding rock are different, which may lead to the emergence of different rock burst evolution and failure processes.

Figure 4 reflects the influence of deflection of principal stress direction on failure mode of surrounding rock. As shown in Figure 4, in the process of tunnel excavation and

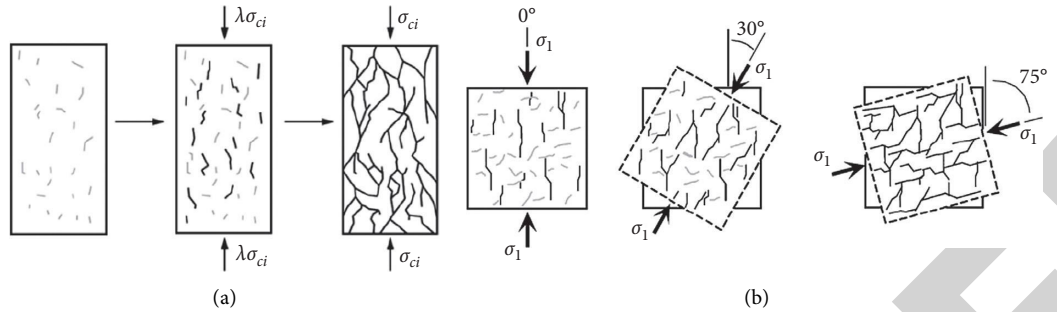

Figure 1: Influence of different stress states on crack propagation. (a) Influence of principal stress ratio on fracture ($1 > \lambda_2 > \lambda_1$). (b) Influence of principal stress direction on fracture [15].

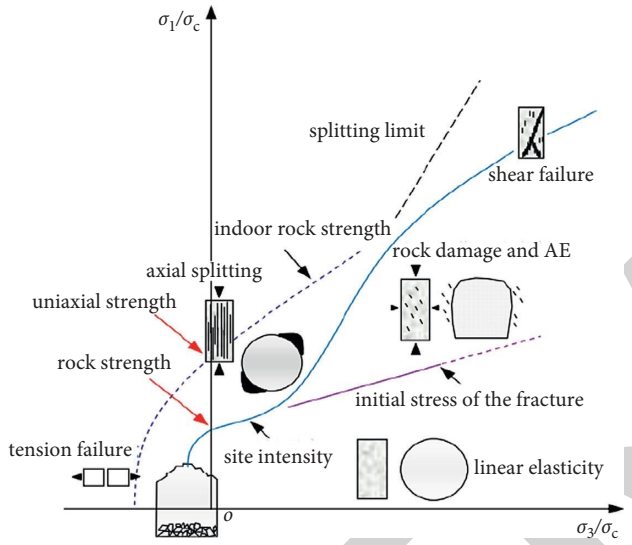

Figure 2: Failure of surrounding rock with different principal stress ratios [15].

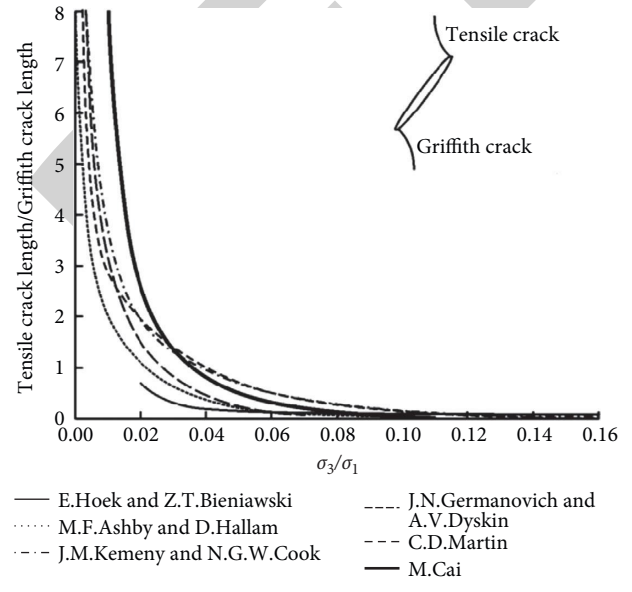

Figure 3: Influence of principal stress ratio on crack mode [14].

unloading, the principal stress direction of the surrounding rock mass will change, and the angle between the stress principal axis of the surrounding rock mass and the micro-cracks will affect the stress field intensity factor at the crack tip. When the principal stress direction of the surrounding rock is at different angles to the micro-cracks, the crack intensity factor presents different ratios. In addition, the direction of stress spindle is a controlling factor of fracture extension direction, and the generation, expansion, and breakthrough of secondary fractures in the surrounding rock mass basically occur along the direction of maximum principal stress, or at a small angle with the direction of maximum principal stress [15].

In summary, the tunnel face to move forward in the process, the surrounding rock by the adit wall to internal on the principal stress ratio increasing, gradient distribution of the tangential stress of surrounding rock will cause different degrees of deflection of the principal stress direction, and the surrounding rock bridge relative to the principal stress direction angle and length will directly affect the deformation and failure mechanism of surrounding rock. Therefore, there must be a correlation between the stress gradient distribution of surrounding rock and rock burst.

2.2. Influence of Stress Gradient Distribution on Principal Stress Ratio and Principal Stress Direction. As shown in Figure 5, during the excavation of underground engineering, the tangential and radial stress of surrounding rock presents gradient stress distribution towards the interior of surrounding rock from excavation unloading, and the difference between them will cause the change of principal stress ratio and principal stress direction of adjacent elements.

In order to study the influence of different stress gradients on the principal stress ratio and principal stress direction of surrounding rock, it is assumed that the axis of the linear underground tunnel is parallel to a principal stress direction in the initial stress field. The vertical stress of excavated rock mass is $\sigma_1 = \sigma$, the horizontal stress is σ_3, and the lateral pressure coefficient $\lambda = \sigma_3/\sigma_1$. The radial stress σ_r, tangential stress σ_θ, and shear stress $\tau_{r\theta}$ of the surrounding rock of the cave wall were calculated by the following formula [16]:

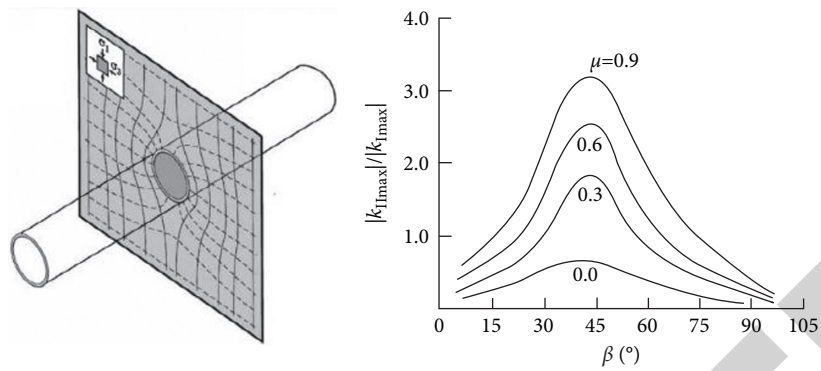

(a) (b)

Figure 4: The change of principal stress direction of surrounding rock and the influence of principal stress direction on intensity factor. (a) Principal stress vector of surrounding rock during tunnel excavation [16]. (b) Influence of principal stress direction on intensity factor [15].

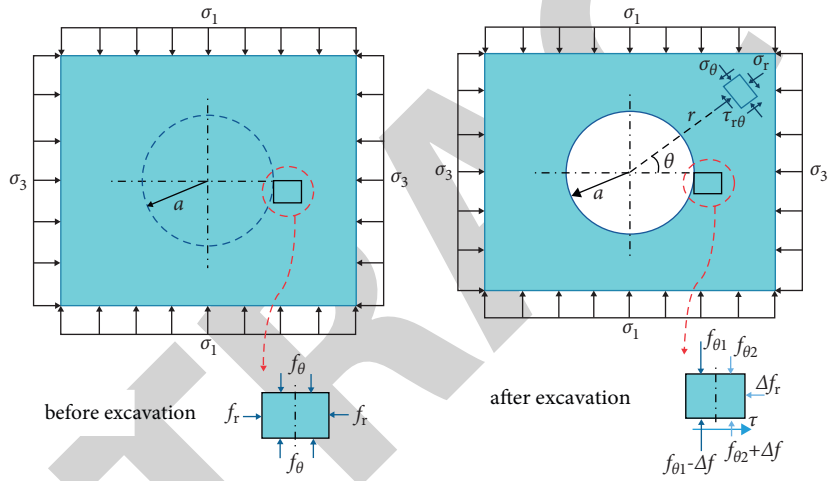

(a) (b)

Figure 5: Stress changes of surrounding rock element before and after model excavation. (a) Stress state of surrounding rock element before model excavation. (b) Stress state of surrounding rock element after model excavation.

$$\sigma_\theta(r,\theta)=\frac{1}{2}\sigma(1+\lambda)\left(1+\frac{a^2}{r^2}\right)+\frac{1}{2}\sigma(1-\lambda)\left(1+\frac{3a^4}{r^4}\right)\cos2\theta, \tag{1}$$

$$\sigma_r(r,\theta)=\frac{1}{2}\sigma(1+\lambda)\left(1-\frac{a^2}{r^2}\right)-\frac{1}{2}\sigma(1-\lambda)\left(1+\frac{3a^4}{r^4}-\frac{4a^2}{r^2}\right)\cos2\theta, \tag{2}$$

$$\tau_{r\theta}=-\frac{1}{2}\sigma(1-\lambda)\left(1+\frac{2a^2}{r^2}-\frac{3a^4}{r^4}\right)\sin2\theta. \tag{3}$$

Formulas (1) and (2) are normalized and then r is derived to obtain the normalized tangential and radial stress change rates of surrounding rock.

Normalized tangential stress gradient change rate:

$$\frac{\partial\sigma_\theta}{\sigma_{\theta\max}\partial r}=\frac{-\left[(1+\lambda)a^2r^2-6(1-\lambda)a^4\cos2\theta\right]}{(1+\lambda)r^5+2(1-\lambda)r^5\cos2\theta}. \tag{4}$$

Normalized radial gradient stress change rate:

$$\frac{\partial\sigma_r}{\sigma_{r\max}\partial r}=\frac{2(1+\lambda)a^2r^2-4(1-\lambda)\left(3a^4-2a^2r^2\right)\cos2\theta}{(1+\lambda)r^5-(1-\lambda)r^5\cos2\theta}. \tag{5}$$

According to formulas (4) and (5), the normalized tangential and radial stress gradients facing the surrounding rock from excavation and unloading are obtained. The tunnel radius is $a=3$ m, and the lateral pressure coefficient λ is 0.3 and 0.5, respectively, for calculation. As the lateral pressure coefficient is less than 1, the damage is mainly concentrated on the two sides of the tunnel. Therefore, the angles θ of 0°, 30°, and 45° are selected as examples to calculate, and the results are shown in Figures 6(a) and 6(b).

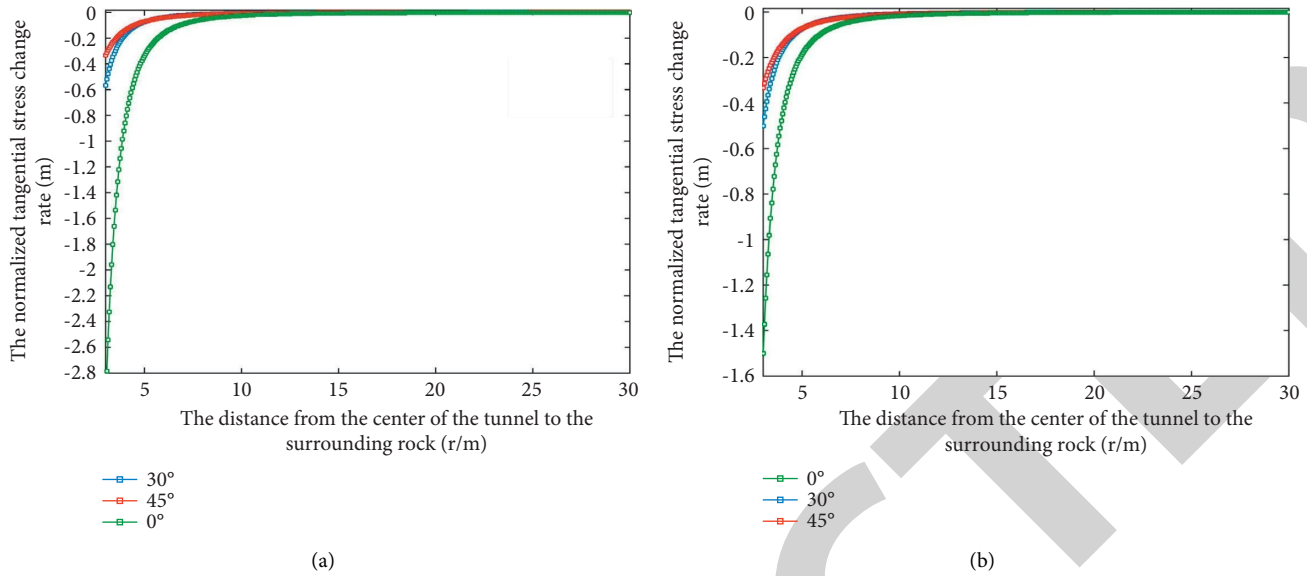

Figure 6: Change rates of tangential stress with different lateral pressure coefficients. (a) Lateral pressure coefficient $\lambda = 0.3$. (b) The lateral pressure coefficient $\lambda = 0.5$.

From Figure 6, the tangential stress change rates of surrounding rock at different angles under different lateral pressure coefficients of circular tunnel can be seen. The tangential stress of surrounding rock gradually decreases from the wall to the inside of surrounding rock, and the change is obvious in the range of 2.5 times tunnel radius ($r = 7.5$ m). Under the same lateral pressure coefficient, the gradient change rate of $\theta = 0^{\circ}$ is the largest, while the gradient change rate of $\theta = 30^{\circ}$ and 45° is smaller. In addition, the comparison between Figures 6(a) and 6(b) shows that the tangential gradient stress change rate of surrounding rock with lateral pressure coefficient $\lambda = 0.3$ is greater than that with lateral pressure coefficient $\lambda = 0.5$ at the same angle, and the smaller the angle is, the more obvious the difference is. It shows that the tangential stress gradient of surrounding rock is related to its position (angle θ) and lateral pressure coefficient.

Figure 7 shows the radial stress change rates of tunnel surrounding rock at different angles under different lateral pressure coefficients.

According to the radial stress change rates of surrounding rock at different angles under different lateral pressure coefficients of circular tunnel in Figure 7, it can be seen that the radial stress change rate of surrounding rock gradually decreases from the tunnel wall to the inside of surrounding rock, and the change is obvious within 2.5 times of the tunnel radius ($r = 7.5$ m). Under the same lateral pressure coefficient, the gradient change rate is the largest at $\theta = 0^{\circ}$, and the radial stress change rate gradually decreases from $\theta = 30^{\circ}$ to 45°, but the difference of radial stress change rate caused by different angles is smaller than the difference of tangential stress at different θ angles. In addition, the comparison of Figures 7(a) and 7(b) shows that the radial gradient stress change rate of surrounding rock with lateral pressure coefficient $\lambda = 0.3$ is greater than that with lateral pressure coefficient $\lambda = 0.5$ at the same angle. The analysis shows that the radial stress gradient of surrounding rock is also related to the position (θ Angle) and lateral pressure coefficient.

In order to discuss the influence of different stress gradients on the principal stress ratio of surrounding rock element, the principal stress of surrounding rock element can be obtained according to the stress conditions of surrounding rock element during excavation:

$$\sigma_1 = \frac{1}{2}(\sigma_r + \sigma_\theta) + \frac{1}{2}\sqrt{(\sigma_r - \sigma_\theta)^2 + 4\tau_{r\theta}^2}, \tag{6}$$

$$\sigma_3 = \frac{1}{2}(\sigma_r + \sigma_\theta) - \frac{1}{2}\sqrt{(\sigma_r - \sigma_\theta)^2 + 4\tau_{r\theta}^2}. \tag{7}$$

According to formulas (6) and (7), the principal stress ratio of surrounding rock stress element can be obtained:

$$\frac{\sigma_3}{\sigma_1} = \frac{(\sigma_r + \sigma_\theta) - \sqrt{(\sigma_r - \sigma_\theta)^2 + 4\tau_{r\theta}^2}}{(\sigma_r + \sigma_\theta) + \sqrt{(\sigma_r - \sigma_\theta)^2 + 4\tau_{r\theta}^2}}. \tag{8}$$

According to formula (8), the change rate of the principal stress ratio from the wall to the interior of the surrounding rock can be obtained by the derivation of r. In this paper, tunnel radius $a = 3$ m, the lateral pressure coefficients λ are 0.3 and 0.5, and the angles θ are 0°, 30°, or 45° are selected as examples for calculation, and the results are shown in Figure 8.

It can be seen from Figure 7 that the change rate of the principal stress ratio from tunnel wall to the interior of surrounding rock tends to the principal stress ratio under the initial ground stress state at a faster rate, that is, the increase rate of σ_3/σ_1 from the tunnel wall to the interior of surrounding rock is faster, and the corresponding principal stress ratio (σ_3/σ_1) of surrounding rock is larger at the same position.

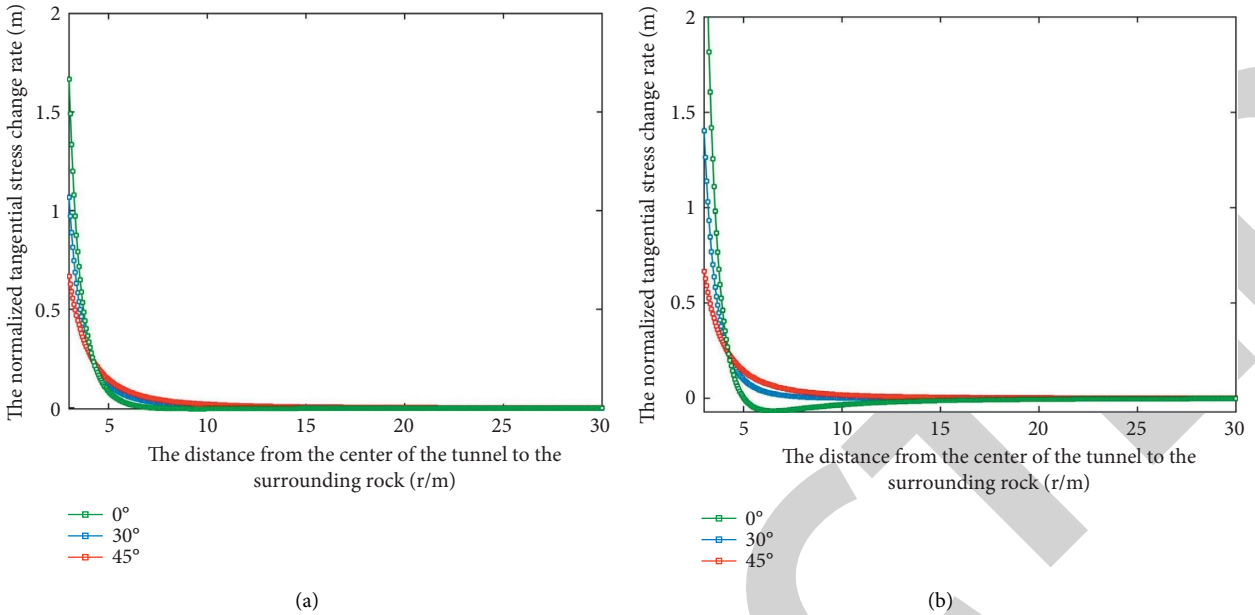

Figure 7: Radial stress change rates under different lateral pressure coefficients. (a) Lateral pressure coefficient $\lambda = 0.3$. (b) Lateral pressure coefficient $\lambda = 0.5$.

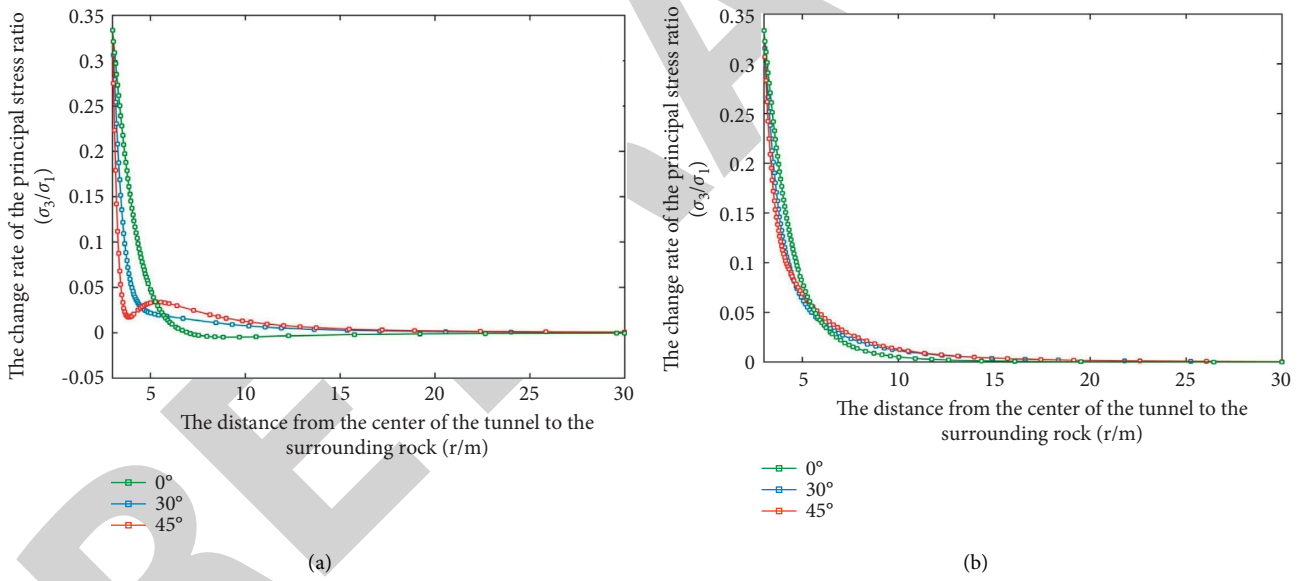

Figure 8: Change rates of principal stress ratio under different lateral pressure coefficients λ. (a) $\lambda = 0.3$. (b) $\lambda = 0.5$.

In order to discuss the influence of different stress gradients on the variation of principal stress deflection angle of surrounding rock element, the rotation angle of principal stress direction of surrounding rock element can be calculated according to the stress condition of surrounding rock element during excavation:

$$\alpha_0 = \frac{1}{2}\arctan\left(\frac{-2\tau_{r\theta}}{(\sigma_\theta - \sigma_r)}\right). \tag{9}$$

By substituting formulas (1)~(3) into formula (9) and differentiating θ, the variation rate of the principal stress deflection angle along the tangential direction of the surrounding rock $\theta = 0^\circ$~45° can be obtained. The lateral pressure coefficients λ 0.3 and 0.5, and the tangential distance between the surrounding rock and the wall $0.3a$ and $0.5a$ are selected as examples for calculation. The corresponding rate of change of the principal stress rotation along the tangential direction of the surrounding rock can be obtained for the surrounding rock stress element, as shown in Figure 9.

It can be seen from Figure 8 that the variation rate of principal stress deflection angle of surrounding rock $r = 0.3a$ and $r = 0.5a$ from the tunnel wall decreases gradually along the tangential $\theta = 0^\circ$~45° range. Under the same lateral pressure coefficient, the variation rate of principal stress

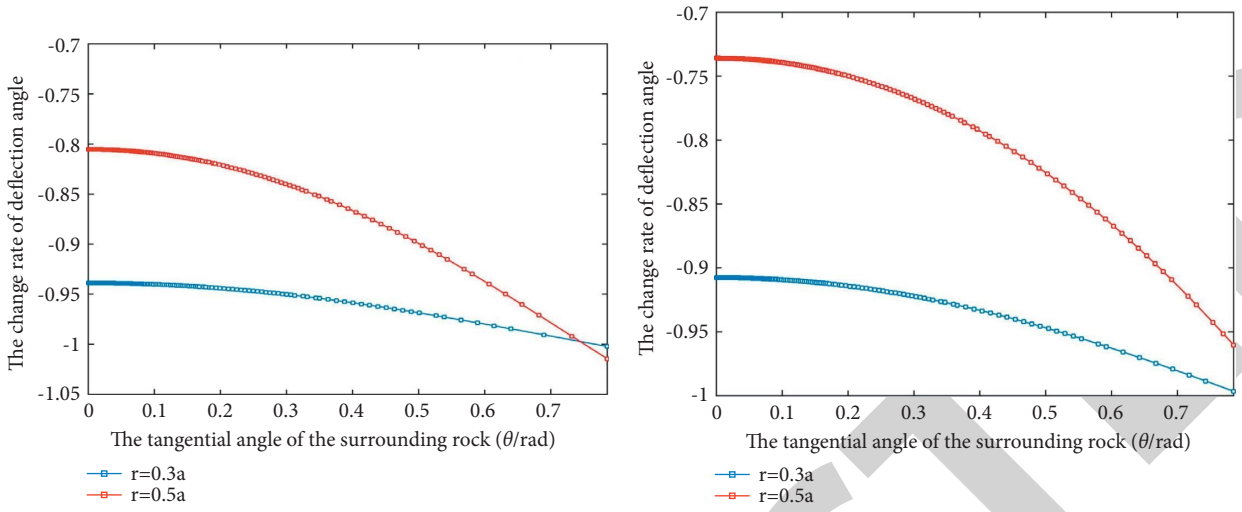

Figure 9: Tangential change rate of principal stress rotation of surrounding rock stress element. (a) $\lambda = 0.3$. (b) $\lambda = 0.5$.

rotation of surrounding rock element near the tunnel wall is generally larger ($r = 0.3a$). In addition, by comparing Figures 8(a) and 8(b), it can be seen that the change rate of principal stress of surrounding rock element with lateral pressure coefficient $\lambda = 0.3$ is generally greater than that of surrounding rock with lateral pressure coefficient $\lambda = 0.5$ for surrounding rock with the same distance from the wall ($r = 0.3a$ or $r = 0.5a$). It shows that when the stress gradient changes greatly, the variation level of principal stress direction of rock mass element in the failure area of surrounding rock is also high.

In summary, it can be seen from the above calculation examples that the stress gradient changes greatly at the two sides of tunnel excavation, and the location where the stress gradient changes greatly, the principal stress ratio, and the change rate of principal stress direction of surrounding rock element near the tunnel wall are generally higher. It shows that the ratio of principal stress of surrounding rock element and the direction of principal stress have a great relation with the stress gradient of surrounding rock.

2.3. Failure Mode Effects' Analysis Based on the Principal Stress Ratio and Principal Stress Direction of the Fracture Criterion of Crack Tip. The stress gradient of surrounding rock is related to the surrounding rock stress ratio and the direction of the principal stress. And the principal stress ratio and principal stress direction have influence on surrounding rock failure mode, both the fracture mechanism of surrounding rock under coupling effect is a problem worthy to be discussed.

After the underground excavation, in the surrounding rock element in the compression state and the crack tip area of stress concentration, the micro-cracks will fracture in the direction of β angle to the maximum principal stress (type I tensile type or type II shear type). In the critical state, the main crack tip stress distribution characteristics actually become the main factors to control the crack propagation and its properties.

Assuming a crack with a length of $2a$ in an infinite rock plate, the edges are subjected to uniformly distributed biaxial pressure σ_1 and σ_3, where $\sigma_1 = \sigma$ *or* $\lambda'\sigma$, λ' is the lateral pressure coefficient and satisfies $0 \le \lambda' \le 1$, the angle between the central crack direction and the σ_1 action direction is β (called crack angle), as shown in Figure 10.

The cracks studied in this paper are closed cracks under compression of surrounding rock, and the friction force caused by the slip of the main crack surface can be given by Coulomb formula, which is given in the coordinate system as shown in Figure 10, that is:

$$\tau = \mu P, \tag{10}$$

$$\tau_{ef} = \begin{cases} (Q - \tau), & (|\tau| \le |Q|), \\ 0, & (|\tau| > |Q|). \end{cases} \tag{11}$$

In the formula: P is the normal reaction pseudo force acting on the crack surface, Q is the tangential reaction pseudo force acting on the crack surface, τ is the friction force caused by the mutual sliding or sliding trend between the upper and lower surfaces of the crack, μ is the friction coefficient on the crack surface, and τ_{ef} is the effective shear stress.

By using the solution of Muskhelishvili complex theory and Riemann Hilbert problem, the basic solution of the crack surface under pseudo force can be obtained as [17, 18].

$$\Phi(z) = \frac{z[-P + i(Q - \tau)]}{2\sqrt{(z^2 - a^2)}}, \tag{12}$$

$$\Omega(z) \frac{z[-P - i(Q - \tau)]}{2\sqrt{(z^2 - a^2)}}. \tag{13}$$

In the formula: $\Phi(z)$ and $\Omega(z)$ are the plane of the complex potential function; z is the independent variable; a is half the length of the cracks.

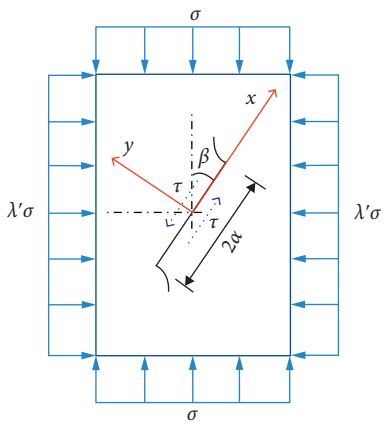

Figure 10: Oblique crack in the center of biaxial compressive stress.

Thus, the stress intensity factor of the main crack tip can be calculated from the following formula:

$$K = K_{\mathrm{I}} - iK_{\mathrm{II}} = 2\sqrt{2}\lim_{z\longrightarrow\pm a}[\sqrt{z \pm a}\,\Phi(z)] = [-P + i(Q-\tau)]\sqrt{\pi a}. \tag{14}$$

In the formula: K_{I} and K_{II} are the stress intensity factors of type I and type II crack tips; $z = \pm a$ are the right and left end points of the crack. From formula (14), it can be seen that the stress strength factor K_{I} and K_{II} of the crack tip are, respectively:

$$K_{\mathrm{I}} = -P\sqrt{\pi a}, \tag{15}$$

$$K_{\mathrm{II}} = -(Q-\tau)\sqrt{\pi a}. \tag{16}$$

In the coordinate system shown in Figure 10, τ is negative (along the negative direction of the x axis). If the compressive stress is positive, then,

$$-P = \frac{1}{2}\sigma(1+\lambda') + \frac{1}{2}\sigma(1-\lambda')\cos 2\beta, \tag{17}$$

$$Q = \frac{1}{2}\sigma(1-\lambda')\sin 2\beta. \tag{18}$$

Thus, the stress intensity factors at the tip of the main crack are, respectively

$$K_{\mathrm{I}} = \left[\frac{1}{2}\sigma(1+\lambda') + \frac{1}{2}\sigma(1-\lambda')\cos 2\beta\right]\sqrt{\pi a}, \tag{19}$$

$$K_{\mathrm{II}} = \left\{-\frac{1}{2}\sigma(1-\lambda')\sin 2\beta + \mu\left[\frac{1}{2}\sigma(1+\lambda') + \frac{1}{2}(1-\lambda')\cos 2\beta\right]\right\}\sqrt{\pi a}. \tag{20}$$

Considering the characteristic of rock compression fracture mode is selective, this chapter uses the Microcrack Cell Model as the basis of analysis of rock compression fracture [15], as shown in Figure 11.

In the figure, $\tau_{\gamma\omega}$ is the shear stress of the crack surface of the tip of the micro-crack element, and σ_ω and σ_γ are the tangential and radial stresses of the crack surface of the tip of the crack element, respectively.

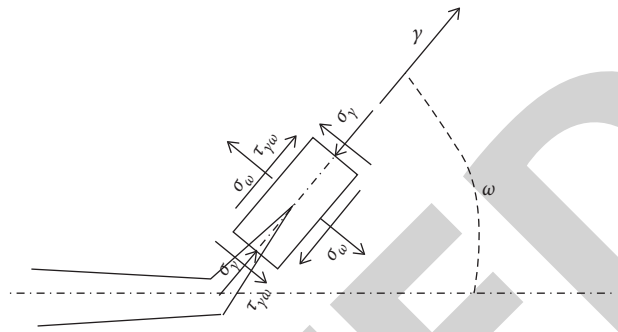

Figure 11: Micro-crack element stress.

Cotterell and Ric [15] gave an approximate formula for calculating the intensity factors K_{I} and K_{II} of type I and type II crack tips, based on the infinitesimally small branch cracks of the planar cracks in Figure 11:

$$\begin{pmatrix} k_{\mathrm{I}} \\ k_{\mathrm{II}} \end{pmatrix} = \begin{pmatrix} c_{11} & c_{12} \\ c_{21} & c_{22} \end{pmatrix}\begin{pmatrix} K_{\mathrm{I}} \\ K_{\mathrm{II}} \end{pmatrix}. \tag{21}$$

Among them,

$$c_{11} = \frac{1}{4}\left(3\cos\frac{\omega}{2} + \cos\frac{3\omega}{2}\right), \tag{22}$$

$$c_{12} = -\frac{3}{4}\left(\sin\frac{\omega}{2} + \sin\frac{3\omega}{2}\right), \tag{23}$$

$$c_{21} = \frac{1}{4}\left(\sin\frac{\omega}{2} + \sin\frac{3\omega}{2}\right), \tag{24}$$

$$c_{22} = \frac{1}{4}\left(\cos\frac{\omega}{2} + 3\cos\frac{3\omega}{2}\right). \tag{25}$$

In the formula: ω is micro-crack propagation angle.

In compression fracture mechanics, only one fracture mode and its corresponding stress intensity factor and fracture toughness cannot be considered in isolation. It is necessary to comprehensively consider who plays a leading role in the tension and shear mechanism, as well as the fracture properties of the corresponding materials. For a closed crack, it is equivalent to [15]:

$$\left|\frac{k_{\mathrm{II}\max}}{k_{\mathrm{I}\max}}\right| \geq K\frac{\prod c}{K_{\mathrm{Ic}}}, \quad \text{Shear fracture,} \tag{26}$$

$$\left|\frac{k_{\mathrm{II}\max}}{k_{\mathrm{I}\max}}\right| \leq K\frac{\prod c}{K_{\mathrm{Ic}}}, \quad \text{tension fracture.} \tag{27}$$

The relative size of the fracture toughness of the material is related to the value of the friction coefficient μ of the crack surface of the material, and the fracture toughness of the model material can be expressed as [19].

$$\frac{K_{\mathrm{II}c}}{K_{\mathrm{I}c}} = \frac{\sqrt{3}\mu}{\sqrt{(\mu^2+1)} - \mu}. \tag{28}$$

The formula (28) is brought into the formulas (27) and (26) to obtain the compression fracture mode criterion. A classification curve for the type of rupture under compressive stress can then be obtained, as shown in Figure 12.

From Figure 12, the plane is divided into two areas according to the classification curve of each friction coefficient in formulas (26) and (27), the tensile failure area on the left side of the curve and the shear failure area on the right. As can be seen from formulas (26) and (27) and Figure 12, for a particular type of rock (friction coefficient is certain, for most rocks, the friction coefficient of the joint surface μ the value range is about 0.5 to 0.9 [20]), and its fracture mode is jointly affected by the coupling of the principal stress ratio and the principal stress direction. Under the action of a large surrounding rock stress gradient, rock compression may occur shear fracture under the action of the surrounding rock reaching a certain crack inclination and appropriate containment pressure.

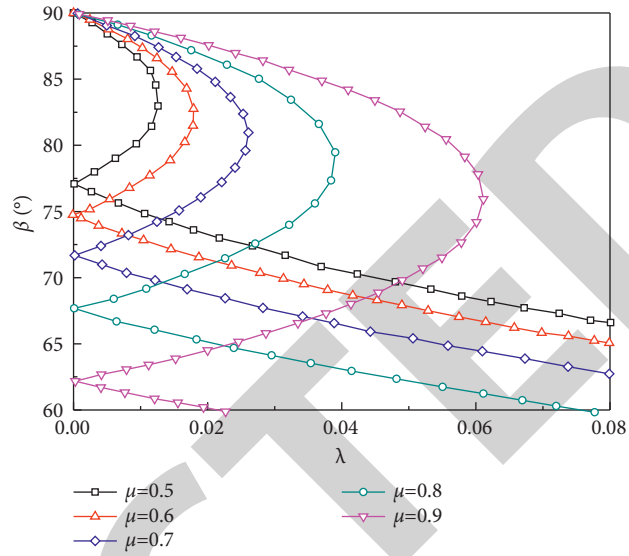

Figure 12: Classification curve of cracking mode of closed crack tip under compressive stress.

3. Project Instance Analysis

3.1. Project Overview. A phosphate mine of the IV section in Yichang is a sedimentary phosphorus block rock deposit, which is deposited in the first section of the Sinian Doushantuo formation, which is a hidden mine. The mine layer has a layered occurrence and monoclinic structure as a whole, and the occurrence is relatively gentle, with a dip of 285°~30° and a dip angle of 2°~9°, gentle in the south, generally 2°~3° in the south, and slightly steep in the north, generally 4°~9°. The IV section of the mine is the deep extension area to the south of the I and III sections of the mine, which belongs to the deep underground mining mine, with a dip angle of 17°~25°, a slow to medium-thick mine body, with a large difference in height along the dip extension, and the type of engineering geological survey is mainly carbonate rock, with a mining depth of 112.67~1021.97 meters and an average depth of 550 meters.

3.2. Lithologic Characteristics of Surrounding Rock. In order to study the crack propagation characteristics of rock burst surrounding rock, this section takes the rock burst phenomenon of a phosphate mine in Yichang as an example. The mine bed of the IV mine section is phosphorite. The type of phosphate rock is determined by energy dispersive spectrometer, and triaxial and uniaxial loading experiments are carried out by hydraulic testing machine to obtain mechanical parameters such as uniaxial strength and elastic modulus of phosphate rock (Table 1). The elemental analysis and uniaxial stress-strain curves of phosphate rock are shown in Figures 13 and 14.

As can be seen from Figure 13, according to the type and content of elements, it can be seen that the sample contains less phosphorus and the grade of the mine is low. The specimen contains less Mg element and more Ca element, so it does not contain dolomite grain, but contains mineral calcite. As can be seen from Figure 14, from the uniaxial stress-strain curve of phosphate rock, the axial stress falls rapidly, the brittleness is obvious, and the lithology of rock burst occurs.

Table 1: Basic physical and mechanical parameters of phosphate rock.

Name	v/	σ_c/MPa	ρ/g·cm^{-3}	E/GPa	φ/°
Phosphate rock	0.26	53.6	2.88	27.1	37.73

Notes: φ-internal friction angle; ρ–density.

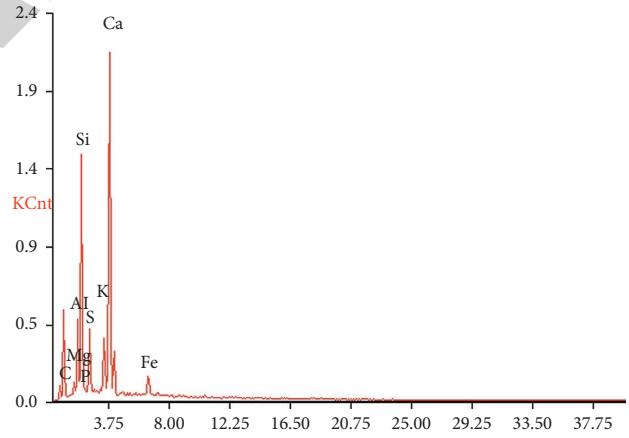

Figure 13: Elemental analysis diagram.

3.3. The Analysis of the Tunnel Surrounding Rock Burst Mode Boundary Curve and Engineering Example. The tunnel section of mine Section 4 is simplified to a circle, the tunnel radius $a = 5$ m, the vertical principal stress of the tunnel $\sigma_1 = 16.2$ MPa, the horizontal main stress $\sigma_3 = 8.43$ MPa, by the analysis of the surrounding rock force of the circular tunnel, from the formula (29), we can obtain the principal

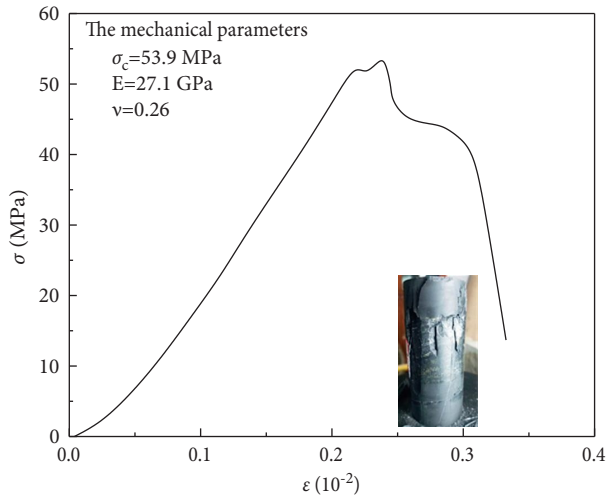

Figure 14: Uniaxial stress-strain curve (E-Young's modulus; ν-Poisson's ratio).

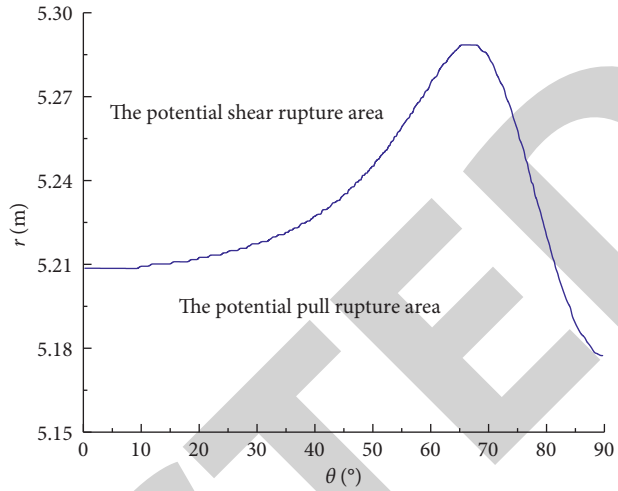

Figure 15: Division of surrounding rock destruction areas.

stress ratio of the circular tunnel surrounding rock element as

$$\lambda' = \frac{(\sigma_r + \sigma_\theta) - \sqrt{(\sigma_r - \sigma_\theta)^2 + 4\tau_{r\theta}^2}}{(\sigma_r + \sigma_\theta) + \sqrt{(\sigma_r - \sigma_\theta)^2 + 4\tau_{r\theta}^2}}. \quad (29)$$

Assuming that the initial micro-cracks will form in the surrounding rock during the tunnel excavation process, and the initial microcracking direction of the surrounding rock is tangential distribution, the angle between the micro-crack direction of the surrounding rock element and the direction of the principal stress σ_1 of the surrounding rock element is β:

$$\beta = |\alpha_0 - \theta| = \left|\frac{1}{2}\arctan\left(\frac{-2\tau_{r\theta}}{(\sigma_\theta - \sigma_r)}\right) - \theta\right|. \quad (30)$$

Suppose that the friction angle φ_0 of the micro-crack surface is equal to the internal friction angle φ of the phosphate rock, where the friction coefficient μ on the crack surface equals to tanφ, according to the triaxial test, the friction angle in the phosphate rock $\varphi = 37.73^\circ$, and then the friction coefficient $\mu = \tan 37.73^\circ = 0.77$ on the crack surface is calculated. K_{IIc}/K_{Ic} is obtained by bringing the $\mu = 0.77$ into formula (28), the micro-crack (length is 2a) of surrounding rock and formula (20) can be obtained by bringing formulas (29) and (30) into formulas (19) and (20), and the stress intensity factors K_I and K_{II} at the tip of infinitesimally small branch cracks can be obtained by bringing K_I and K_{II} into formula (22). The fracture mode demarcation curve of surrounding rock after circular tunnel excavation can be obtained by bringing K_I,K_{II}, K_{IIc}/K_{Ic} into formulas (6) and (7), as shown in Figure 15. Figure 16 shows the analysis of fracture mode in in-situ rock burst failure areas.

The lateral pressure coefficient of tunnel in IV mining section is $\lambda = \sigma_3/\sigma_1 = 0.52$, and the overall β value varies little, so the fracture mode of surrounding rock element is mainly affected by the principal stress ratio of surrounding rock element. It can be seen from the failure of the surrounding rock explosion in Figure 16(a) that the maximum failure depth of the surrounding rock (0.15 m) appears in the part of $\theta = 0^\circ$, and the failure depth of upper and lower beam roof decreases gradually along the tangential direction, and the failure is within the range of $\theta = -30^\circ \sim 30^\circ$. The maximum depth of rock burst failure is 0.15 m less than the potential tensile failure depth of the theory $\theta = 0^\circ$ in Figure 14 ($r(\theta = 0^\circ) - a \approx 0.21$ m), indicating that the rock burst failure area in Figure 16(a) is within the potential tensile failure area in Figure 15. The results of scanning electron microscope (SEM) of typical fracture surface in Figure 16(a) show that there are delamination cracks parallel to the observation plane on the micro-crack surface, which is an intergranular rough type "I" tensile crack, indicating that the fracture in the rock burst area is consistent with the theoretical potential fracture area. As can be seen from the rock burst failure of surrounding rock in Figure 16(b), the maximum failure depth of the surrounding rock (0.25 m) appears in the part of $\theta = 0^\circ$, and the failure depth of upper and lower beam roof decreases gradually along the tangential direction, and the failure is within the range of $\theta = \pm 30^\circ$. The maximum depth of rock burst failure is 0.25 m, which is greater than the potential tensile failure depth of the theory $\theta = 0^\circ$ in Figure 15 ($r(\theta = 0^\circ) - a \approx 0.21$ m), indicating that most of the rock burst failure area in Figure 16(a) is within the potential tensile failure area in Figure 15, and a small part of the rock burst failure area is located in the potential shear fracture area in the range of $\theta = 0^\circ$ (about 0.25 – 0.21 = 0.04 m). The results of scanning electron microscopy (SEM) of the typical fracture surfaces of the two failure areas in Figure 16(b) show that there is a delaminated exfoliated crack parallel to the observed surface on the micro-crack surface, which is an intergranular rough type I tensile crack without shear fracture characteristics. It illustrates that the theoretical potential fracture area basically reflects the fracture characteristics of actual rock burst in the surrounding rock. The maximum failure depth (0.34 m) of surrounding rock at $\theta = 10^\circ$in Figure 16(c) is greater than the potential tensile failure depth

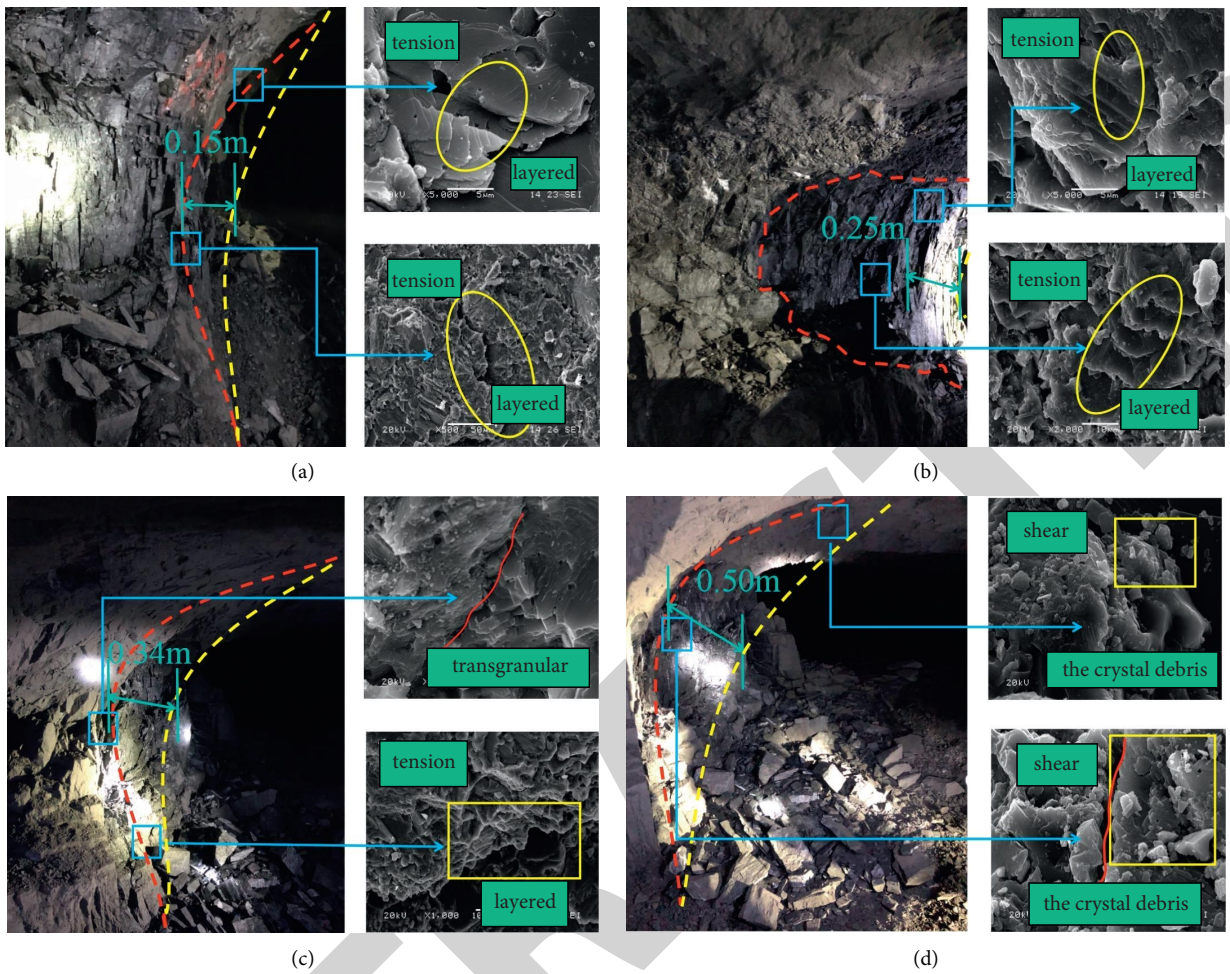

Figure 16: A phosphate rock burst failure area in Yichang, Hubei Province and surrounding rock fracture surface scanning electron microscopy. (a) Rock burst section 1. (b) Rock burst section 2. (c) Rock burst section 3. (d) Rock burst section 4.

of $\theta = 10^{\circ}(r(\theta = 0^{\circ}) - a \approx 0.21$ m) in Figure 15, and the failure area spans both tensile and shear areas. The detritus at the bottom of the rock burst pit (potential shear failure area) can be seen by scanning electron microscope that there is a clear curved crack on the visible crystal surface, which is not straight, which is a transgranular shear crack, and the scanning electron microscope at the edge of the crater (potential tensile failure area) shows the characteristics of tensile fracture. The maximum failure depth (0.5 m) of the surrounding rock in Figure 16(d) at $\theta = 20^{\circ}$ is greater than the potential tensile failure depth ($r(\theta = 0^{\circ}) - a \approx 0.21$ m) in Figure 15, and the failure area spans both tensile and shear areas. However, the results of the SEM scans for different areas are all shear-breaking features in Figure 16(d).

Comparing the results of the area of surrounding rock fracture mode of the rock burst in the field with the theoretical potential fracture mode zoning, it can be seen that the division of fracture mode of surrounding rock does not completely correspond to the fracture mode of the actual surrounding rock corresponding failure area. However, the division of the surrounding rock failure mode area can predict the surrounding rock fracture mode to a certain extent. In addition, because the limited sampling of scanning electron microscopy and the samples are only obtained in the rock burst pit, it is not possible to completely determine whether the actual surrounding rock failure mode boundary is consistent with the theoretical value.

4. Conclusions

The influence of the gradient distribution of the surrounding rock element due to excavation on the fracture mode of the surrounding rock during the rock burst is analyzed. The evolution process of fracture mode of surrounding rock is deeply analyzed from the perspective of stress change before and after excavation. The results show that:

(1) The tangential and radial stress rates of the surrounding rock are larger at the wall, and gradually tend to 0 towards the interior of surrounding rock, and are mainly concentrated in the radius of 2.5 times the tunnel. When the lateral pressure coefficient $\lambda < 1$, the overall rate of change of the tangential and radial stress gradients from the wall to the interior of the surrounding rock is larger on both sides of the tunnel ($\theta = 0^{\circ}$), and the overall rate of change of

the stress gradient along the tangential direction of the tunnel to the upper and lower roof ($\theta = \pm 90^{\circ}$) decreases.

(2) The surrounding rock element is affected by the gradient stress, and the larger stress gradient corresponds to the surrounding rock with a larger principal stress ratio and the direction of the principal stress change. The surrounding rock fracture mode is jointly affected by the coupling of the principal stress ratio and the principal stress direction. Under the action of certain crack inclination angle and appropriate confining pressure (principal stress ratio), different fracture mechanisms (type I tensile, type II shear) may occur in the compression of the surrounding rock.

(3) Based on theoretical analysis, the potential fracture mode of different areas of the surrounding rock of a phosphate mine mining in Yichang are estimated, and compared with the fracture characteristics of the surrounding rock of the actual rock burst section, the theoretical results can predict the fracture characteristics of the surrounding rock at the site to a certain extent.

Data Availability

Some or all data, models, or code that support the findings of this study are available from the corresponding author upon reasonable request.

Conflicts of Interest

The authors declare that they have no conflicts of interest.

Acknowledgments

The authors sincerely thank the financial support from the National Natural Science Foundation of China (no. 52079098), the Fundamental Research Funds for the Central Universities (no. 2042022kf1219), the Collaborative Innovation Center for Prevention and Control of Mountain Geological Hazards of Zhejiang Province (no. PCMGH-2021-03), and the Hubei Key Laboratory of Roadway Bridge and Structure Engineering (Wuhan University of Technology) (no. DQJJ202104).

References

[1] X. Liu, Y. Xia, and M. Lin, "Experimental study of rockburst under true-triaxial gradient loading conditions," *Geomechanics and Engineering*, vol. 18, no. 5, pp. 481–492, 2019.

[2] X. Liu, Y. Xia, M. Lin, G. Wang, and D. Wang, "Experimental study on the influence of tangential stress gradient on the energy evolution of strainburst," *Bulletin of Engineering Geology and the Environment*, vol. 80, no. 6, pp. 4515–4528, 2021.

[3] M. Lin, L. Zhang, and X. Liu, "Microscopic analysis of rockburst failure on specimens under gradient stress," *Rock and Soil Mechanics*, vol. 41, no. 9, pp. 2984–2992, 2020.

[4] G. Su, J. Jiang, S. Zhai, and G. Zhang, "Influence of tunnel Axis stress on strainburst: an experimental study," *Rock Mechanics and Rock Engineering*, vol. 50, no. 6, pp. 1551–1567, 2017.

[5] S. Huang, "Study on mechanical model of brittle rock under high stress condition and its engineering application," *The Chinese Academy of Sciences Wuhan*, Institute of Rock & Soil Mechanics, China, 2008.

[6] L. P. Liu, X. G. Wang, Y. Z. Zhang, Z. X. Jia, and Q. W. Duan, "Tempo-spatial characteristics and influential factors of rockburst: a case study of transportation and drainage tunnels in Jinping II hydropower station," *Journal of Rock Mechanics and Geotechnical Engineering*, vol. 3, no. 2, pp. 179–185, 2011.

[7] M. Wang, Y. H. Niu, and Y. Yu, "Experimental research on characteristics of deformation and failure of surrounding rock of roadway in deep mine under influence of principal stress evolution," *Chinese Journal of Geotechnical Engineering*, vol. 38, no. 2, pp. 237–244, 2016.

[8] K. Zhao, H. Y. Zhao, and Q. Y. Jia, "Ananalysis of rockburst fracture micro morphology and study of its mechanism," *Explosion and Shock Waves*, vol. 35, no. 6, pp. 913–918, 2015.

[9] S. Tang Tang, C. Bao, and H. Liu, "Brittle fracture of rock under combined tensile and compressive loading conditions," *Canadian Geotechnical Journal*, vol. 54, no. 1, pp. 88–101, 2017.

[10] L. Liu, X. Wang, and Z. Jia, "Experiment study of marble mechanical properties of Jinping II hydropower station under complex loading and unloading conditions," *Rock and Soil Mechanics*, vol. 34, no. 8, pp. 2287–2294, 2013.

[11] D. C. Wang, *Study on Failure Evolution Mechanism and Control of Roadway Driving along Next Goaf in Fully Mechanized Top Coal Caving Face in Kilometer Deep mine*, Shandong University, Jian, China, 2015.

[12] L. Song, G. Wang, X. Wang et al., "The influence of joint inclination and opening width on fracture characteristics of granite under triaxial compression," *International Journal of Geomechanics*, vol. 22, no. 5, Article ID 04022031, 2022.

[13] Y. Luo, G. Wang, X. Li et al., "Analysis of energy dissipation and crack evolution law of sandstone under impact load," *International Journal of Rock Mechanics and Mining Sciences*, vol. 132, Article ID 104359, 2020.

[14] Z. Y. Li, G. Wu, and T. Z. Huang, "Variation of energy and criteria for strength failure of shale under traixial cyclic loading," *Chinese Journal of Rock Mechanics and Engineering*, vol. 37, no. 3, pp. 662–670, 2018.

[15] W. Cui and N. Wang, "Principal stress axis rotation and effect on failure model of surrounding rock during tunnelling," *Journal of Central South University*, vol. 45, no. 6, pp. 2062–2070, 2014.

[16] B. L. Wang and Y. W. Mai, "Fracture of a piezoelectric material layer bonded by two elastic layers," *International Journal of Engineering Science*, vol. 40, no. 15, pp. 1697–1727, 2002.

[17] J. P. Shi, M. Xie, and J. Wang, "Compression and shear fracture analysis of slanting cracks in infinite planes," *Engineering Mechanics*, vol. 23, no. 12, pp. 59–63, 2006.

[18] A. X. Zheng and X. Q. Luo, "Research on combined fracture criterion of rock under compression-shear stress," *Rock and Soil Mechanics*, vol. 36, no. 7, pp. 1892–1898, 2015.

[19] B. T. Pan and H. M. Tang, "The characteristics of the compression-shera frac-ture in rocks and the I-IIcomposite fracture," *Earth Science*, vol. 13, no. 4, pp. 413–421, 1988.

[20] B. Xu and J. J. Jiang, "Study of I-II mixed mode fracture criteria for concrete," *Engineering Mechanics*, vol. 12, no. 2, pp. 13–21, 1995.